nature electronics

Supplementary information

https://doi.org/10.1038/s41928-024-01194-0

Pressure-stamped stretchable electronics using a nanofibre membrane containing semi-embedded liquid metal particles

In the format provided by the authors and unedited

This PDF file includes:

Materials

Thermoplastic polyurethane (TPU, Elastollan 2180A10) was purchased from BASF. Liquid metal (EGaIn, Ga:In mass ratio of 75.5:24.5) was purchased from Dingguan Metal Technology Co. Hexafluoroisopropanol (AR) and poly(vinyl alcohol) (PVA 1788) were purchased from Aladdin Chemistry Co., Ltd. Polyacrylonitrile (PAN) was purchased from Aldrich Chemical Co., Inc. Poly(vinylidene fluoride-co-hexafluoropropylene) (PVDF-HFP, Kynar Flex 280) was purchased from Arkema Inc. Sylgard 184 was provided by Dow Corning. N,N-dimethylformamide (DMF), acetone and anhydrous ethanol were purchased from Sigma-Aldrich and used without further purification. Deionized water was utilized throughout the experiments. Mouse epithelioid fibroblasts (L929) cells were obtained from the cell bank of the Type Culture Collection Committee of the Chinese Academy of Sciences.

Characterizations

Finite element analysis

Finite element simulations were carried out by COMSOL Multiphysics software with Solid Mechanics module. TPU Young's modulus was set to 10 MPa and Poisson's ratio was set to 0.35 at a density of 1.330 g/cm^3. For the LM particle, the Poisson's ratio was set to 0.499, the density to 6.25 g/cm^3, and the dynamic viscosity to 1.99 MPa/s. The Young's modulus was set to E_1 = 8.32 MPa, E_2 = 3.025 MPa and E_3 = 0.758 MPa according to three simplified conditions discussed previously.

Microstructure characterization

The surface morphology of LMNM samples was characterized by SEM (Regulus 8230). The surface elemental distribution (including C and Ga) of the samples was characterized by energy-dispersive X-ray spectroscopy (EDS, EVO 18). The material surfaces were characterized using X-ray photoelectron spectroscopy (XPS, Thermo Scientific EXCALAB 250 XI).

Mechanical property characterization

The mechanical properties of LMNM and TPU fibres were evaluated using an electronic tensile testing machine (Instron). Long strips of 50 mm × 10 mm were cut from the samples for testing. The change in sample resistance during stretching was measured using a Keithley DMM6500 connected to a computer, and the 4-terminal method was used to accurately measure the resistance change of the samples and avoid interference. The sample strips were clamped to the stretching machine, and the ends of the sample were fixed with conductive silver paste and highly conductive copper tape. Alligator clips were used to connect the machine to the copper tape at the ends of the sample.

Electrical property characterization

To determine the electrical properties of LMNM, the sample square resistance was measured using a four-probe tester (Suzhou Jingge Electronic Co. LTD., M-3) and the sample resistance was measured using a Keithley DMM6500.

The conductivity(σ) of the LMNM circuit can be calculated through the Equation:

$$\sigma = \frac{l}{R \cdot w \cdot t}$$

where l, w, t and R are the length, width, thickness and resistance of the LMNM circuit, respectively. The resistance of the LMNM circuit was determined to be 0.112 Ω, based on the average of five samples with dimensions of 10 mm in length and 2 mm in width. The thickness, measured from SEM cross-section images, was found to be approximately 21 μm. The conductivity of the LMNM circuit was calculated to be 2.13 $\times 10^6$ S m^{-1}.

For skin contact impedance measurements, two 15 mm × 30 mm long strips were applied to the inner side of the left arm, with a distance of 5 cm between the centers of the two samples. Before application, the inner arm was scrubbed with ethanol to ensure proper skin contact. Commercial gel electrode (Junchen Guangzhou Co. Ltd.) was used as control group.

Electro-luminescence

To create electroluminescent circuits, ZnS electroluminescent powder (Shanghai Keyan Optoelectronics Co., Ltd.) was added to uncured PDMS and stirred before being coated onto the fibre surface of the stamped circuit. The coated circuit was then covered with a transparent conductive PET film after curing. AC of 100 V and 3 kHz was applied between the circuit and the conductive PET film to activate the electroluminescent powder.

Photothermal effect characterization

The samples were irradiated using a near-infrared (808 nm) laser (LR-MFJ-808, Changchun Laser Technology Co., Ltd.) at a fixed distance of 10 cm. The temperature

of the sample is obtained in real-time through a thermocouple fixed on the back of the sample, and the temperature changes of the sample are recorded using a commercial infrared camera (FLIR ONE Pro, FLIR Systems, Inc.) during irradiation.

Moisture permeability and Water vapor transmission (WVT) rate characterization

The moisture permeability of the samples was determined in accordance with ASTM E96/E96M-2012 textile standard. The test was conducted at 32°C and 50% relative humidity for a duration of 24 hours. The samples were closely sealed over the mouth of a cup containing water and placed in the test environment. The weight loss of water was measured during this time to determine the mass of water vapor that permeated the samples.

For the test of water vapor transmission (WVT) rate, a wide-mouth bottle was filled with 50 ml of DI water and weighed accurately as M_{0h}. The samples were completely sealed over the mouth of the bottle, which was then placed at 37°C and 75% humidity for 24 hours. The weight of the bottle and samples were recorded as M_{24h}. A same bottle without any membrane served as the control ($M_{control}$). The water vapor transmission (WVT) rate was calculated using the following equation:

$$\text{WVT rate (\%)} = \frac{M_{0h}-M_{24h}}{M_{0h}-M_{control}} \times 100\%$$

Air permeability

Air permeability was measured by using a fully automatic permeability instrument (YG461G, Ningbo Dahe Instrument Co., Ltd., China) according to the ASTM D737-75 standard test method under varied pressure drops. The output airflow rate (in units of mm/s) represents the air permeability of samples.

Collection of ECG and EMG signals

To collect ECG signals, the commercial ECG monitor (Heal Force PC-80B) was connected to the copper tape at the samples. Three 2 cm × 10 cm strip shaped LMNM were prepared and a 2×2 cm^2 area of the inner side was activated for conductivity. The

inner conductive area was led out using copper tapes to facilitate the connection of wires, and the copper tapes were wrapped with parafilm to avoid direct contact with skin. Three samples were placed on the left wrist, right wrist, and left ankle using medical tape. A commercial gel electrode (Junchen Guangzhou Co. Ltd.) was used for the control group. The artificial sweat was prepared according to ISO 3160-2 standard, including 20 g/L sodium chloride (NaCl), 17.5 g/L ammonium chloride (NH_4Cl), 5 g/L urea, 2.5 g/L acetic acid (CH_3COOH), 15 g/L lactic acid, 80 g/L sodium hydroxide (NaOH) for adjusting the pH value to 4.7, and DI water.

To measure muscle EMG signals, the MyoWare Muscle Sensor was used. LMNM samples (2×2 cm^2) were connected to the electrodes of the biosensor with copper tapes, and copper tapes were sealed with parafilm to avoid direct contact with skin.

The tests on human skin were approved by the Ethics Committee of Soochow University (approval number: SUDA20210929H01) and received informed consent from the volunteer subject.

Cell cytotoxicity characterization

To evaluate the cytotoxicity, L929 fibroblasts were chosen as model mammalian cells. The viability and morphology of cells cultured on different surfaces were assessed using live/dead staining assay. DAPI was used to stain demarcated cells, and PI was used to stain dead cells. The samples were imaged using a fluorescence microscope (Leica DM2500 Microscope) with excitation filters in front of a mercury metal halide lamp. After 24 hours of culture, most cells were attached, and all cells were stained green. Very few cells were stained red, indicating a high level of cell viability. The cells displayed a normal and healthy spindle shape morphology. Additionally, cell proliferation was evaluated using a quantitative Cell Counting Kit-8 (CCK-8) assay.

All the samples were sterilized under ultraviolet light for 30 min and then placed in 24-well plates. L929 cells were seeded to each well at a density of 50,000 cells/well in 1 ml of 1640 medium supplemented with 10% FBS and incubated for 12 h at 37 °C in a humidified 5% CO_2 atmosphere. Following this, 100 μL of CCK-8 dye was added to each well and the plates were incubated for an additional 2 h at 37 °C. The absorbance

was measured using a multifunctional microplate reader at 450 nm wavelength, and untreated cells were used as controls. The cell viability (%) was then estimated from the readings obtained:

$$cell\ viability = \frac{A_s - A_b}{A_c - A_b} \times 100\%$$

Where A_s represents the absorbance of the experimental group in which the cells are incubated with samples. A_b and A_c are the absorbances of the blank and control groups, respectively. Each sample was measured with five parallel wells.

Wettability characterization

The wettability of LMNM prepared by different polymers were tested by Dataphysics optics contact Angle measurement (OCA25, Germany). Deionized water was used as the test liquid, the volumes of the droplets were fixed to 1.5 μl.

Supplementary Discussion

Sedimentation rate of LM particles in solution

During the spinning process, the Reynolds number value of the spinning solution was low, indicating that the inertial force was much smaller than the viscous force. As a result, the viscous force played a dominant role, allowing the inertial force to be completely ignored, making it applicable to Stokes' flow[1,2]. The LM particles were primarily subjected to gravity and the resistance of the solution. In this context, we disregarded the electrostatic force generated by the charge accumulation on the LM particles.

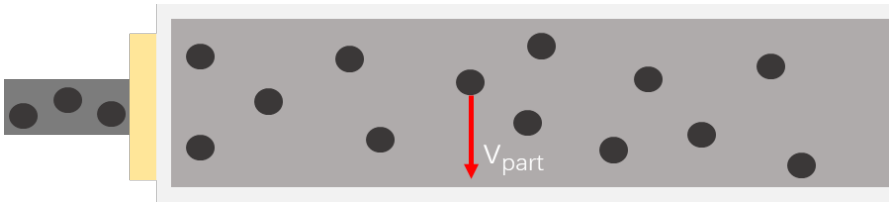

Considering the buoyancy of the solution on the LM particles, the force generated by gravity was

$$F_{gravity} = (\rho_{particle} - \rho_{fluid}) \times \frac{4}{3}\pi r^3 g \quad (1)$$

where $\rho_{particle}$ is the density of the LM particle (6.25 g/cm^3, ignoring the oxide layer), ρ_{fluid} is the density of the solution, r is the radius of the LM particle, and g is the acceleration of gravity. The drag force on the LM particle can be calculated using Stokes' law as follows.

$$F_{drag} = 6\pi\eta r V_{rel} \quad (2)$$

where η is the viscosity of the solution and v_{rel} is the relative velocity between the solution (V_{fluid}) and the LM particle (V_{part}).

$$V_{rel} = V_{fluid} - V_{part} \quad (3)$$

Since the solution flow velocity was very small (only 1 ml h^{-1}), we consider the solution flow velocity to be zero. In this case, the settling velocity of the LM particle in solution can be solved by ordering $F_{gravity}$ and F_{drag} to be equal.

Using a TPU spinning solution with an LM content of 40 wt% as an example (with a density of 1.924 g/cm³, a viscosity of 497 mPa·s, and LM particles radius of 0.495 μm), we calculated the sedimentation velocity of the LM particles in the spinning

solution to be 4.62×10^{-6} cm/s. In a 10 ml syringe with an inner diameter of 1.5 cm for electrospinning, the time for LM particle to settle from the middle of the syringe to the bottom was over 40 hours. However, a single electrospinning process typically lasts less than 20 hours. By rotating the syringe several times during the electrospinning, we ensured the even distribution of LM particles in the solution throughout the process.

Effective modulus and selection of LM particles in TPU nanofibres

For small size LM particles coated with polymeric nanofibres, the effective modulus E_P can be predicted using a generalized Eshelby theory[3,4,5]:

$$E_P = E_0 \frac{24\frac{\Upsilon}{E_0 R}}{10+9\frac{\Upsilon}{E_0 R}} \qquad (4)$$

The surface tension of the LM (γ) is 0.624 N/m, and the modulus of the polymer (E_0) is 10 MPa for the TPU used. The particle radius is denoted by R.

We simplified the presence of LM particles in nanofibres to three cases based on the relationship between the radius of LM particle (R_P) and the radius of nanofibres (R_{Fibre}):

i) $R_P \leq \frac{1}{2} R_{Fiber}$: LM particle is completely embedded in the nanofibre. We set the LM particle radius R_1 to 0.18 μm. The effective modulus E_1 of LM particle is calculated to be 8.32 MPa, which is close to the effective modulus of TPU.

ii) $\frac{1}{2} R_{Fiber} < R_P < 3R_{Fiber}$: LM particle size is similar to the fibre size. We set the LM particle radius R_2 to 0.495 μm. The effective modulus E_2 of the LM particle is calculated to be 3.025 MPa. At this time, the LM particle can still be immobilized by the polymer nanofibres, but due to the existence of the position bias, the LM particle can break through the limitation of the polymer and overflow out.

iii) $R_P \geq 3R_{Fiber}$: We set the LM particle radius R_3 at this time to be 1.975 μm, and the effective modulus E_3 of the LM particle at this time is 0.758 MPa. However, due to the large size difference, such LM particles are difficult to be electrospun and immobilized by polymer fibres.

Considering the feasibility of stamping and electrospinning, as well as the overall stability of the nanofibre membrane, we chose LM particles that meet the second situation for use.

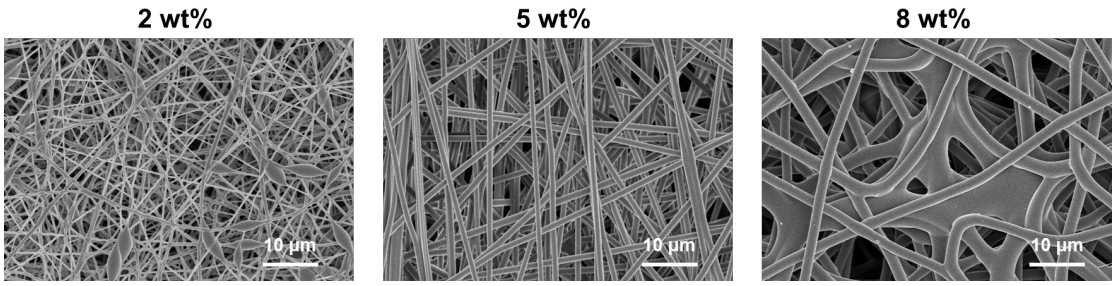

Supplementary Fig. 1 | SEM images of electrostatically spun nanofibres at different TPU solution concentrations. Low solution concentration (2 wt%) leads to beading phenomenon and poor uniformity of nanofibres. While the too high concentration (8 wt%) makes it difficult for the solution to stretch and separate into uniform fibres. Therefore, maintaining a concentration of 5 wt% addresses these issues and facilitates the successful formation of uniform TPU nanofibres.

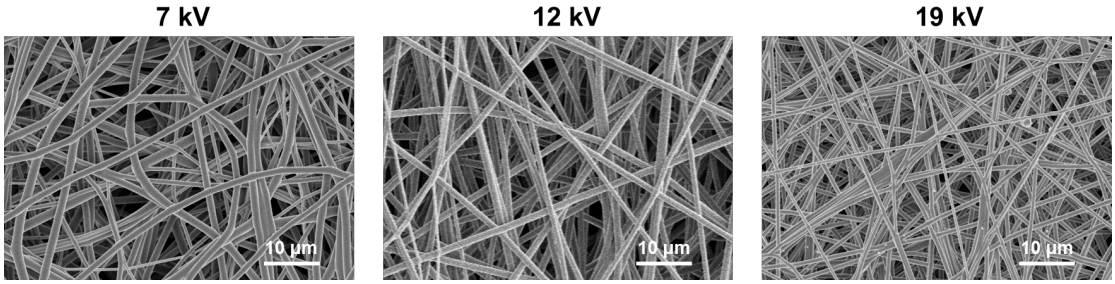

Supplementary Fig. 2 | SEM images of electrostatically spun nanofibres at different applied voltages. When the electrostatic repulsion from the surface charge of the polymer fluid exceeds the surface tension of the solution, the polymer solution will jet flow. At low voltage (7 kV), the jet flow is unstable and the stretching of the solution droplets is inadequate, resulting in poor nanofibre uniformity. Conversely, high voltage (19 kV) can lead to instability of the Taylor cone and fibre adhesion. Therefore, to achieve the desired nanofibre quality and uniformity, the selection of the applied voltage is critical, and based on our findings, a voltage of 12 kV is optimal.

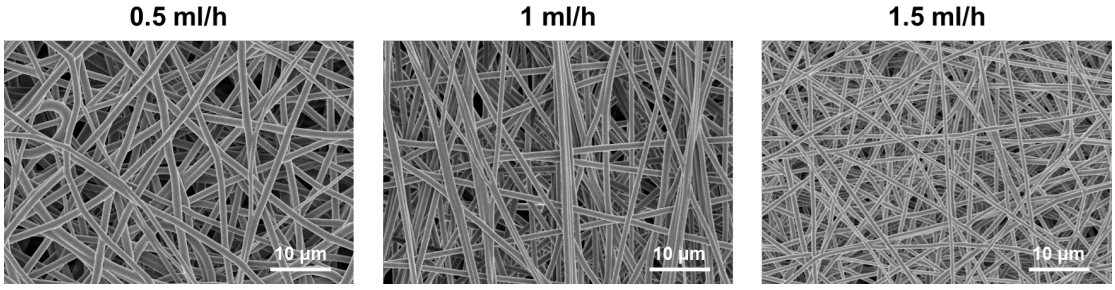

Supplementary Fig. 3 | SEM images of electrostatically spun nanofibres at different TPU solution flow rates. At a low flow rate of 0.5 ml/h, it becomes challenging for the Taylor cone to stably exist, and there is a risk of it retracting into the tip. Conversely, a high velocity of 1.5 ml/h would result in secondary separation of the jet flow, leading to reduced fibre diameter and overall instability of the jet. Therefore, our research supports the contention that a solution flow rate of 1 ml/h offers the best compromise in this experimental setup.

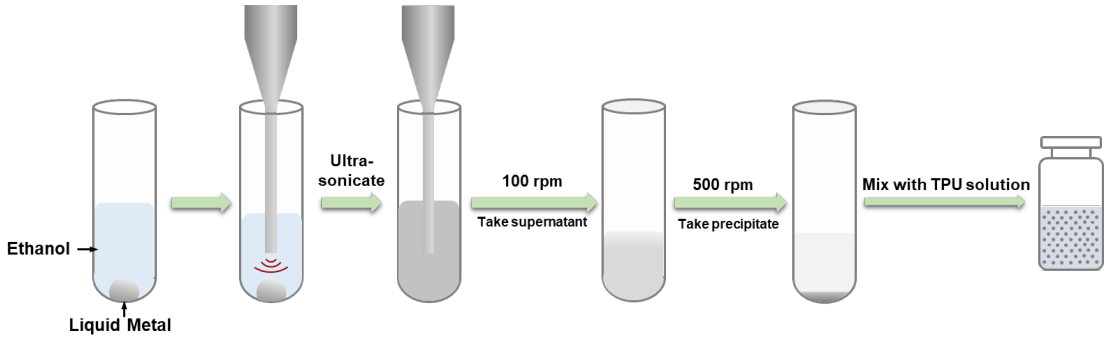

Supplementary Fig. 4 | Schematic diagram of the LMNM precursor solution preparation process. The LM particles were obtained by sonicating 1 g of EGaIn eutectic alloy in 5 g of anhydrous ethanol in a 10 ml centrifuge tube for 5 min at 50% power in an ultrasonic cell disruption system. The centrifuge tube was placed in an ice water bath during the process. The obtained LM slurry was centrifuged at 1 g for 60 seconds and the supernatant was retained. The centrifugation was continued at 27g for 90 seconds, and the supernatant was carefully removed. The LM slurry at the bottom was then mixed with the TPU solution and stirred at room temperature for 2 hours to achieve uniform dispersion of the particles in the solution.

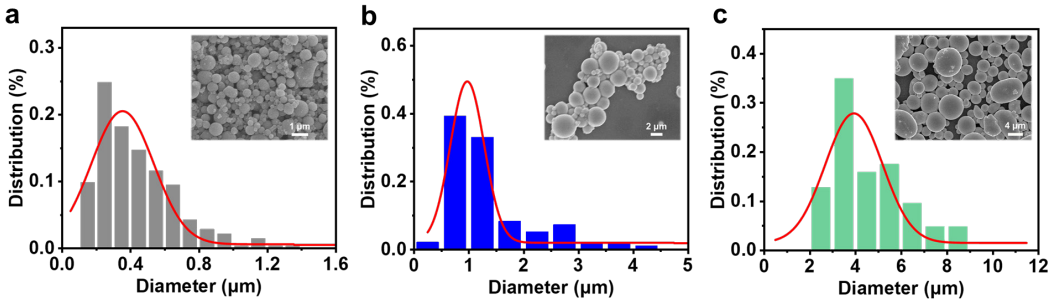

Supplementary Fig. 5 | Diameter distribution of LM particles with different sizes. The LM slurry obtained by ultrasonic cell crushing system can be separated into LM particles of different sizes by centrifugation at different speeds and vacuum drying at room temperature. (**a**) Small size LM particles. Obtained by vacuum drying the supernatant after centrifugation at 27 g for 90 seconds. (**b**) Medium sized LM particles. The supernatant after centrifugation at 1 g for 60 seconds was further centrifuged at 27 g for 90 seconds, keeping the lower layer precipitation and vacuum dried. (**c**) large size LM particles. Obtained by vacuum drying the precipitation after centrifugation at 1 g for 60 seconds. The mean diameters obtained by Gaussian fitting are 0.36 μm, 0.99 μm, and 3.95 μm, respectively.

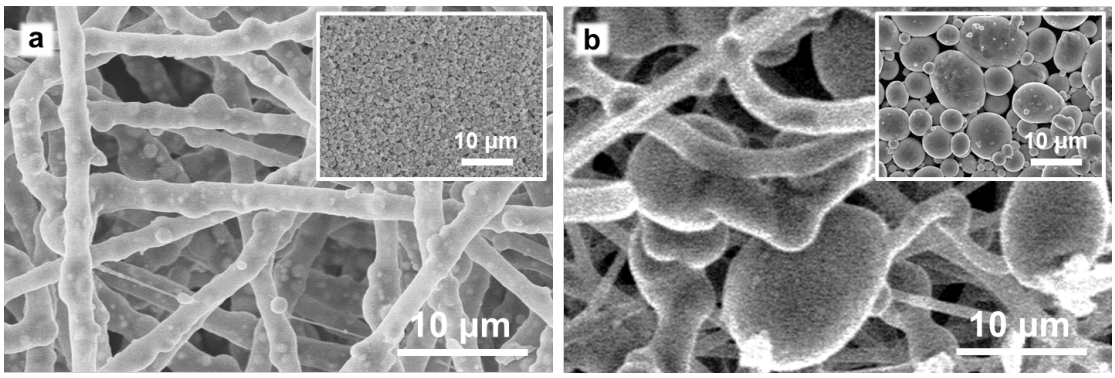

Supplementary Fig. 6 | SEM images of LMNM. LMNM with fully-embedded LM particles (**a**) and overloaded LM particles (**b**). LM particles with small sizes are fully embedded in the nanofibres and cannot escape under pressure, while oversized LM particles are difficult to combine with nanofibres stably and can even break the continuity of fibres, greatly reducing the mechanical properties of nanofibre membranes. Insets are SEM images of LM particles used.

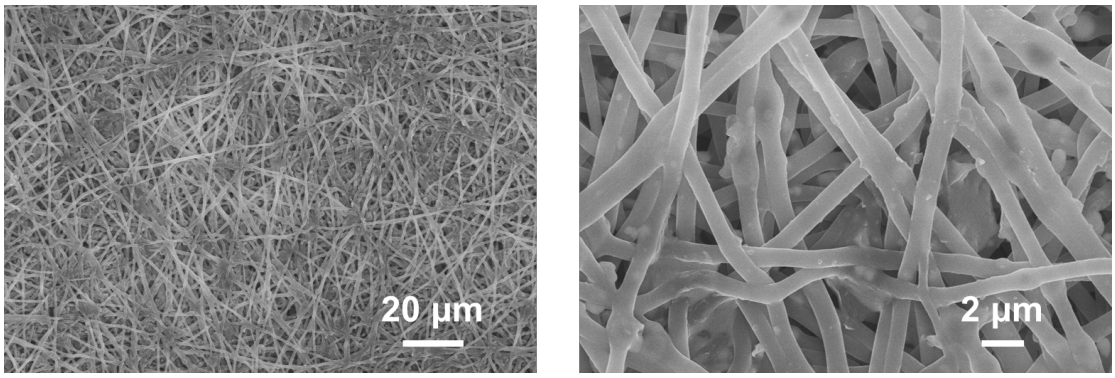

Supplementary Fig. 7 | SEM images of LMNM with fully-embedded LM particles after pressure-stamping. LM particles with too small particle size are fully embedded in the nanofibres, and their relative modulus is too large even after stamping, it is difficult to spill out from the polymer and can not form conductive pathways as effectively as semi-embedded LM particles.

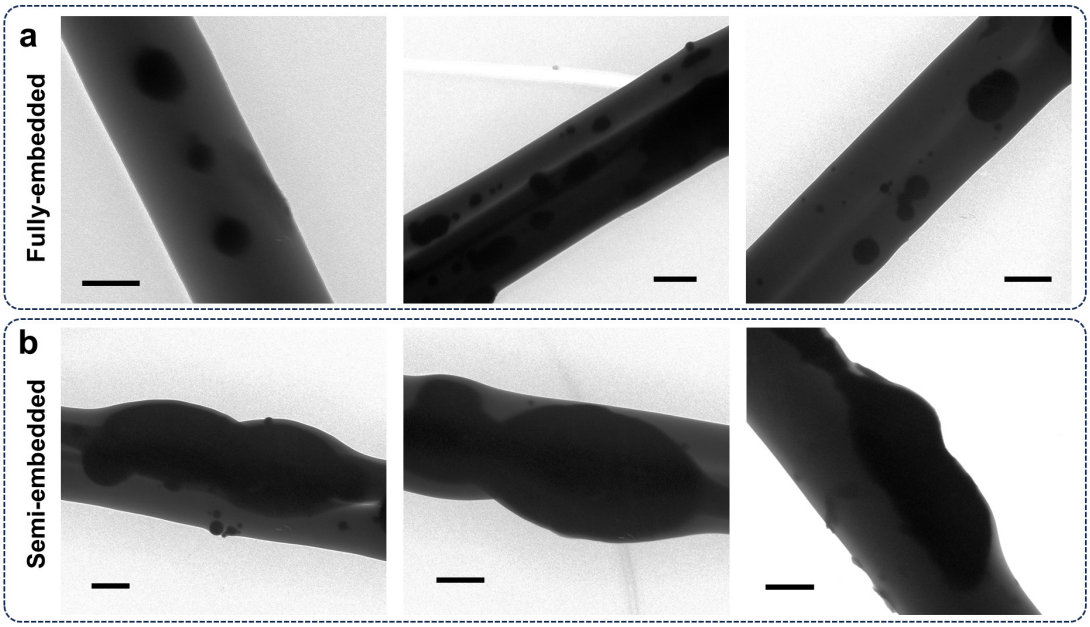

Supplementary Fig. 8 | TEM images of LMNM with different embedded forms of LM particles. (**a-c**) fully-embedded; and (**d-f**) semi-embedded LMNM. Scale bar: 500 nm.

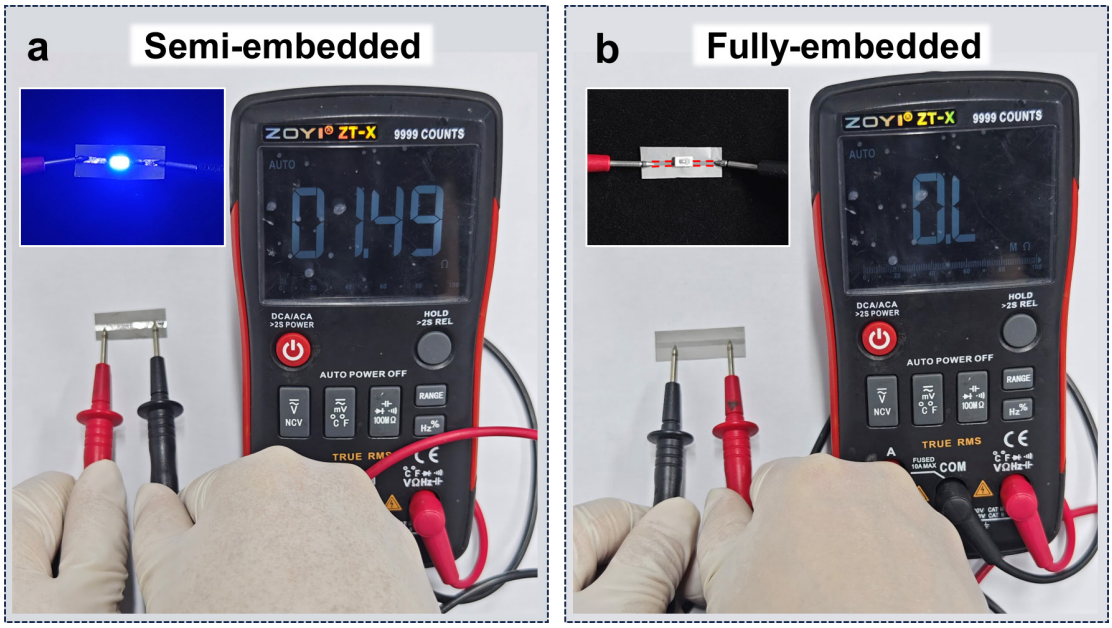

Supplementary Fig. 9 | Resistances and conduction conditions of fully-embedded and semi-embedded LMNM after stamping. (**a**) Semi-embedded LMNM can be activated by the stamping process, while (**b**) fully embedded LMNM cannot.

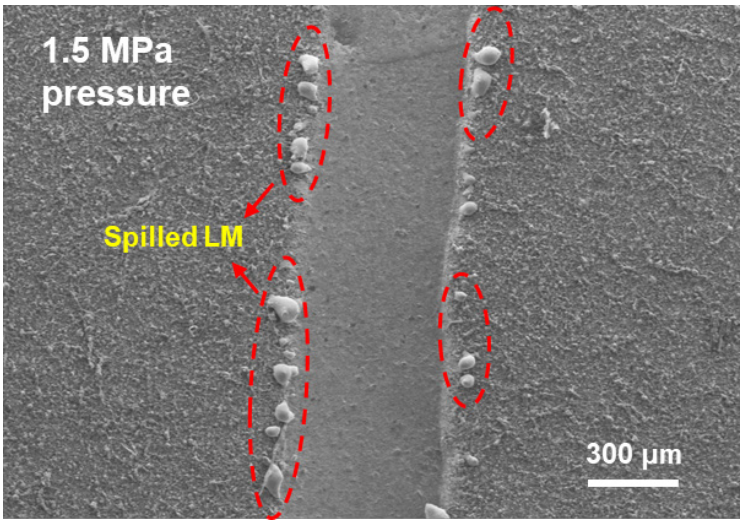

Supplementary Fig. 10 | SEM image of LMNM under 1.5MPa pressure. Excessive pressure further compresses the gap between nanofibres, causing the incompressible liquid metal to migrate laterally to the outer regions, decreasing the effective thickness and LM content of the conductive area, leading to an increase in resistance.

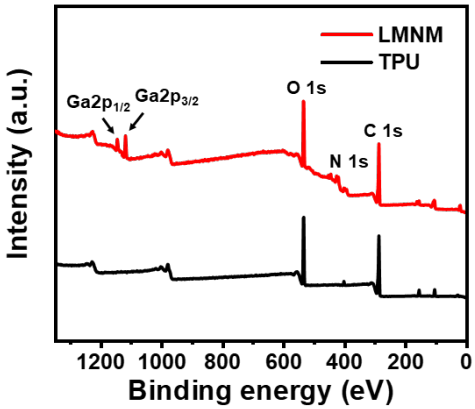

Supplementary Fig. 11 | XPS spectral analysis. XPS full spectra of LMNM and TPU, peaks at 1118 eV and 1145 eV are respectively assigned to $Ga2p_{3/2}$ and $Ga2p_{1/2}$, confirming the existence of LM in LMNM.

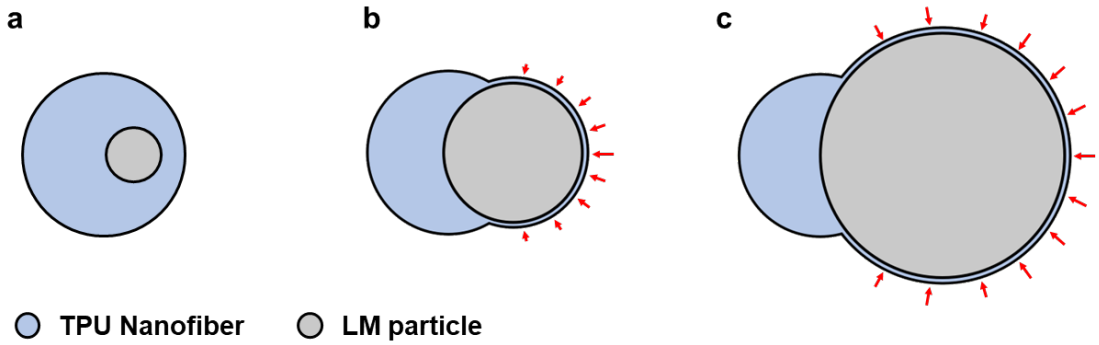

Supplementary Fig. 12 | Schematic representation of three possible scenarios of LM particles in TPU nanofibres. (**a**) LM particle is completely embedded in the nanofibre with a radius of R_1=0.18 μm, leading to an effective modulus of E_1=8.32 MPa, nearly the Young's modulus of TPU. (**b**) LM particle size is similar to the fibre size R_2=0.495μm, with a calculated effective modulus of E_2=3.025 MPa. Although still immobilized by the polymer nanofibres, the LM particle can break through the limitation of the polymer and overflow out due to the position bias. **c**, LM particle size is much larger (R_3=1.975 μm) than the fibre size, leading to an effective modulus of E_3=0.758 MPa. Due to the significant size difference, such LM particles are difficult to electrospun and immobilized by polymer fibres, potentially causing the rupture of polymer fibres. The nanofibre diameters were all set to 1.17 μm. Red arrows indicate the possible locations of the rupture point.

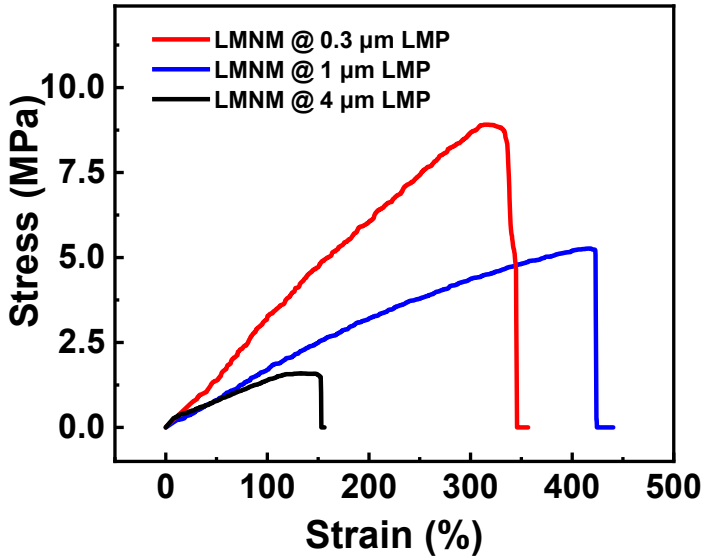

Supplementary Fig. 13 | Mechanical properties of LMNM containing LM particles with different particle sizes. LM particles with average size of about 0.3 µm was completely embedded inside the nanofibres, resulting in an increase in the modulus and a decrease in the elongation at the break of the LMNM. The LM particles with average particle size of about 1 µm matched the nanofibre size and had excellent overall mechanical properties. The LM particles with average particle size of about 4 µm is too large, resulting in excessive defects inside the nanofibres and a substantial decrease in mechanical properties.

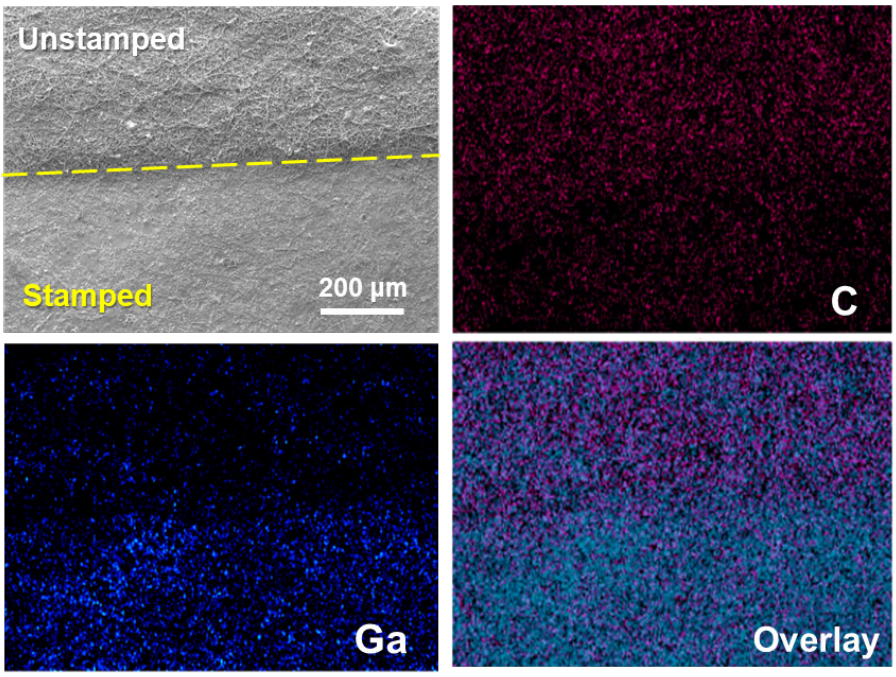

Supplementary Fig. 14 | SEM micrographs and element mappings of LMNM at the junction of the stamped area. LM particles at the stamped area ruptured, filled and covered the voids of TPU nanofibre network while the polymer fibres can still be observed. Significant differences in the distribution of carbon (C) and gallium (Ga) element abundances can be seen from the mapping images. The signal intensity of Ga (representing LM of the stamped area) is higher and more continuous than the C (representing polymer), just opposite to the unstamped area.

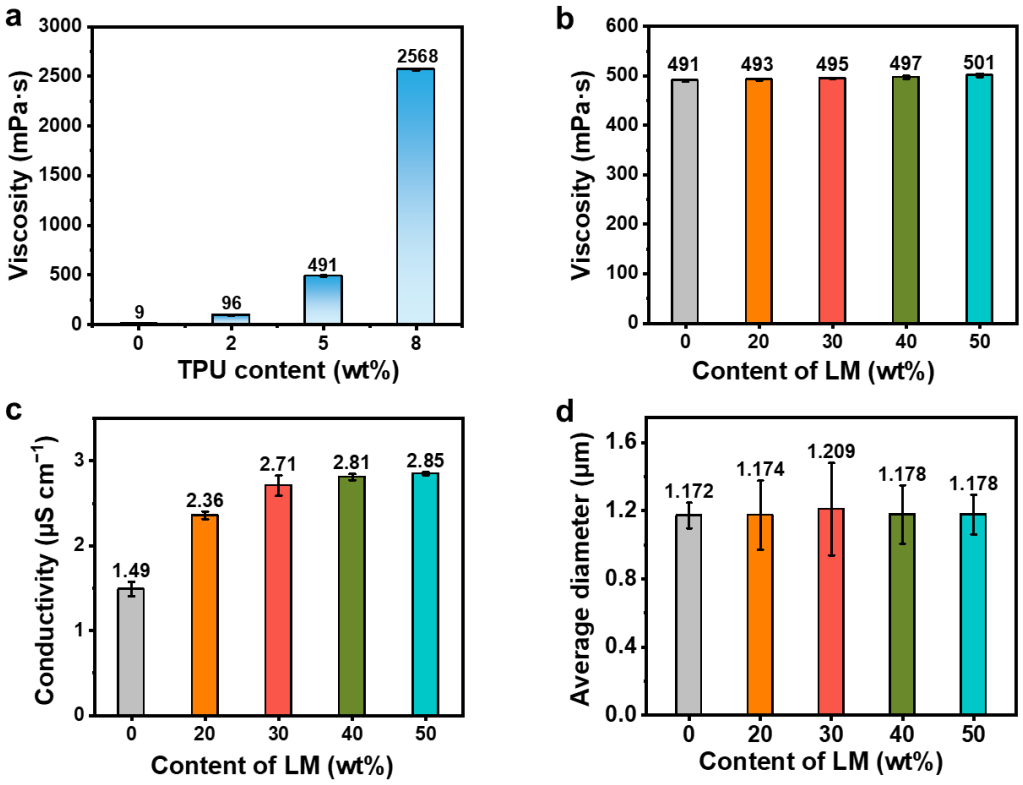

Supplementary Fig. 15 | Viscosity and conductivity of electrospinning precursor solution and diameter of the resulting nanofibres. (**a**) Viscosity of electrospinning precursor solution at different TPU content. (**b**) viscosity, (**c**) conductivity of electrospinning precursor solution and (**d**) diameter of electrospinning nanofibres at different LM content. The addition of LM particles did not significantly affect the viscosity and conductivity of the electrospinning precursor solution or the diameter of the resulting nanofibres. Data are presented as mean values ± s.d. (n = 5 biologically independent samples).

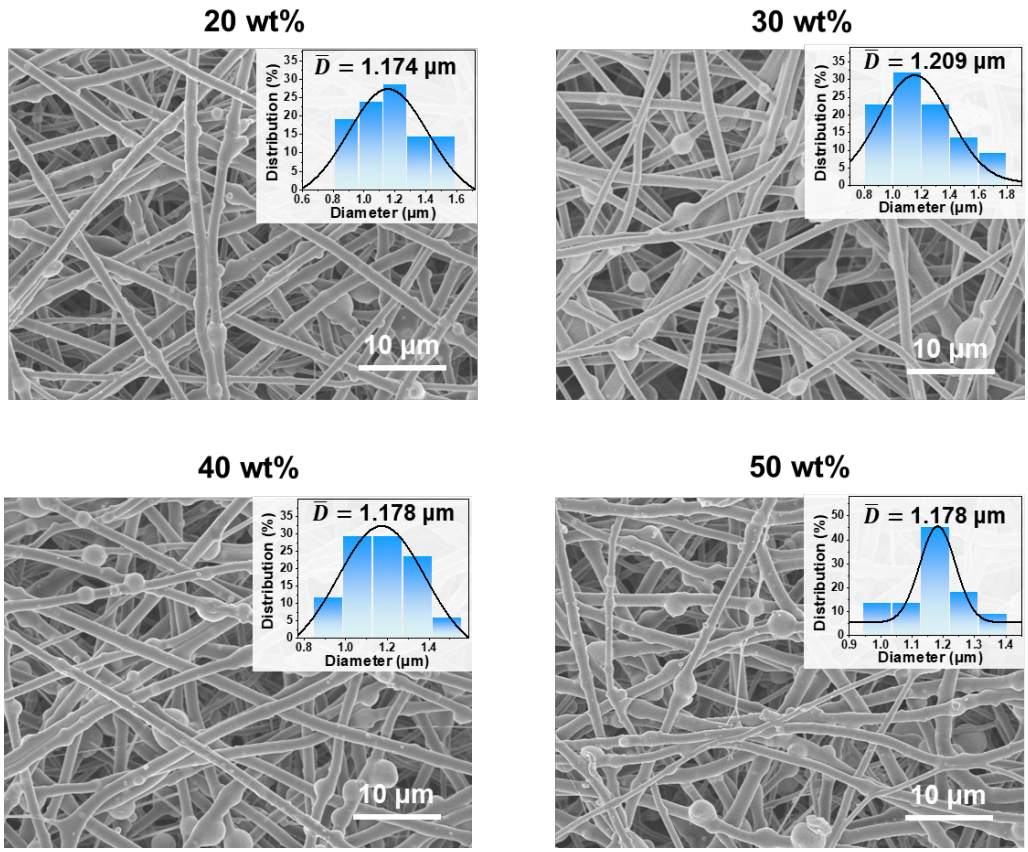

Supplementary Fig. 16 | SEM images and diameter distributions of electrospinning nanofibres at different LM content. The influence on the diameter of prepared nanofibres can be ignored when adding different content of LM particles.

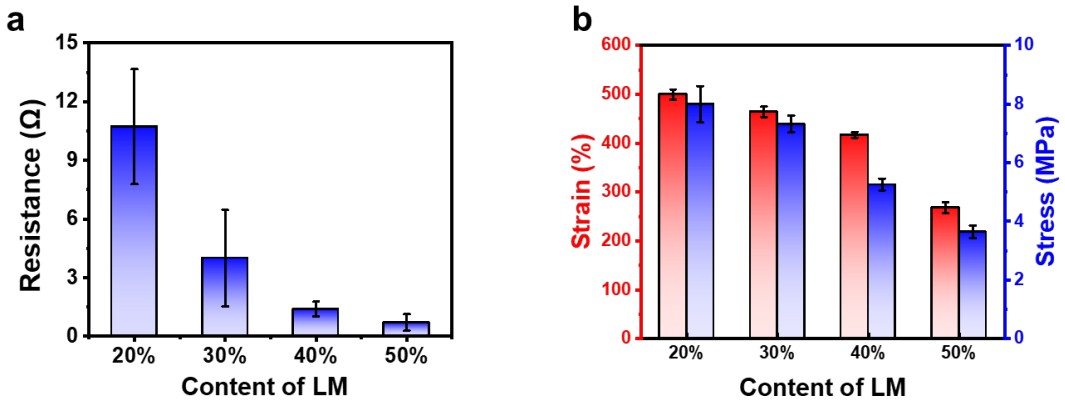

Supplementary Fig. 17 | Resistance and Mechanical properties of LMNM with different LM contents. Histogram of (**a**) resistance-strain and (**b**) maximum strain and stress of LMNM with different LM contents. With the increase of LM content, the conductivity of LMNM increases and the mechanical properties decrease. Considering both electrical and mechanical properties, we chose LMNM with 40 wt% LM as the research object. Data are presented as mean values ± s.d. (n = 5 biologically independent samples).

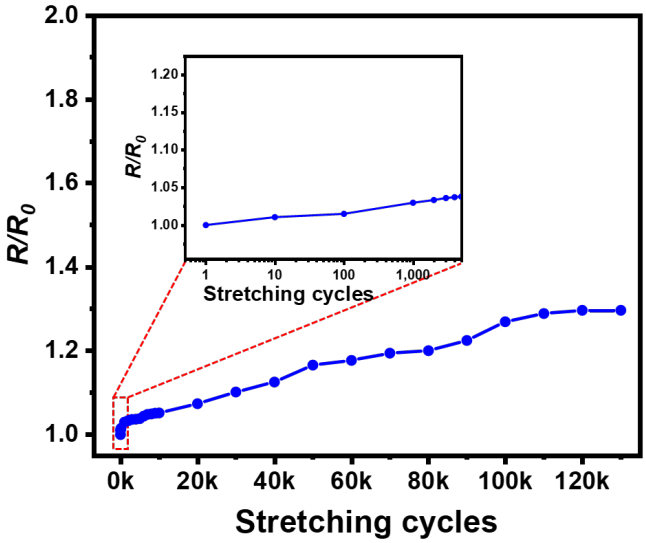

Supplementary Fig. 18 | Cyclic tensile stability of LMNM. Resistance changes of LMNM after undergoing 120,000 tensile cycles at 100% tensile strain. R and R_0 represent the resistance after stretching and before stretching, respectively. The LMNM shows good stability with only a small increase in resistance after cycling, indicating excellent mechanical durability.

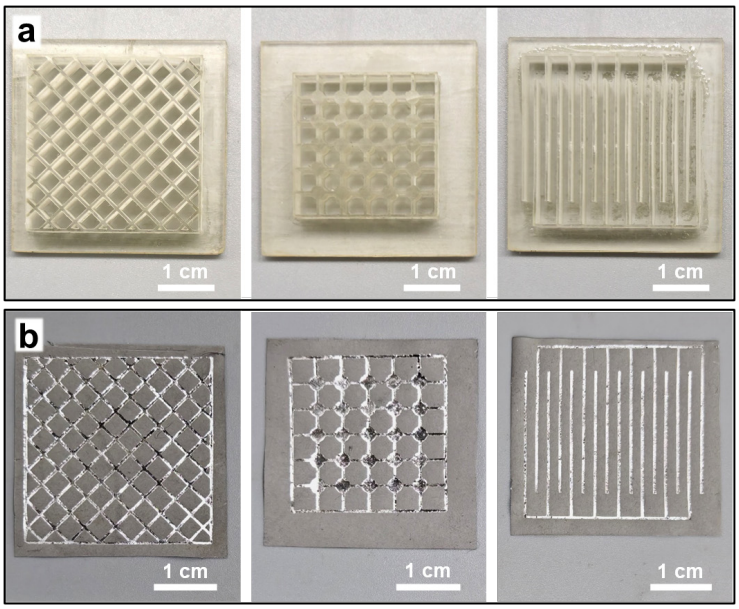

Supplementary Fig. 19 | Multiple patterned circuits based on LMNM. (**a**) Templates prepared by 3D printing for stamping and (**b**) their corresponding patterned electrodes stamped on LMNM.

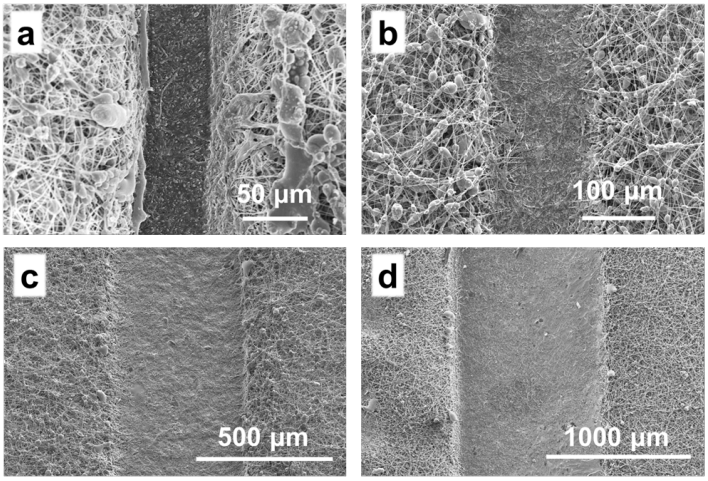

Supplementary Fig. 20 | Different stamped LM line widths. SEM images of LMNM with (**a**) 50 µm, (**b**)100 µm, (**c**) 500 µm, and (**d**) 1000 µm stamped line width.

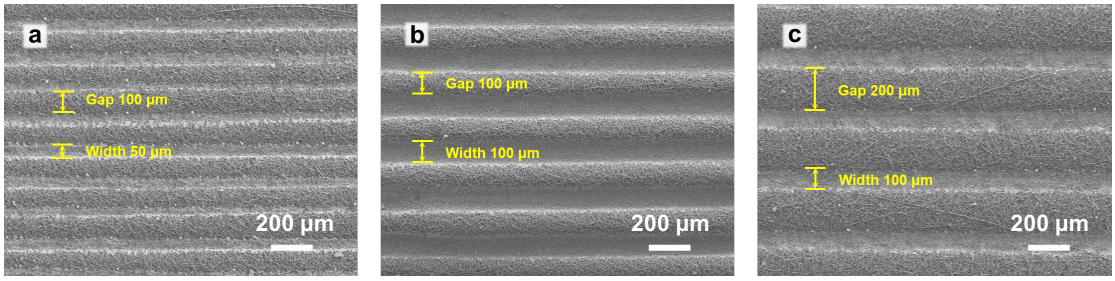

Supplementary Fig. 21 | Different stamped LM line widths and spacing. SEM images of LMNM with (a) 50 μm line width and 100 μm spacing, (b) 100 μm line width and 100 μm spacing, (c) 100 μm line width and 200 μm spacing. All samples were analyzed using a semiconductor parameter analyzer (Agilent B1500 A) in conjunction with a probe station (Lakeshore CRX-4K). The resistances between adjacent lines were measured to be greater than 1 MΩ, and no short circuit was detected.

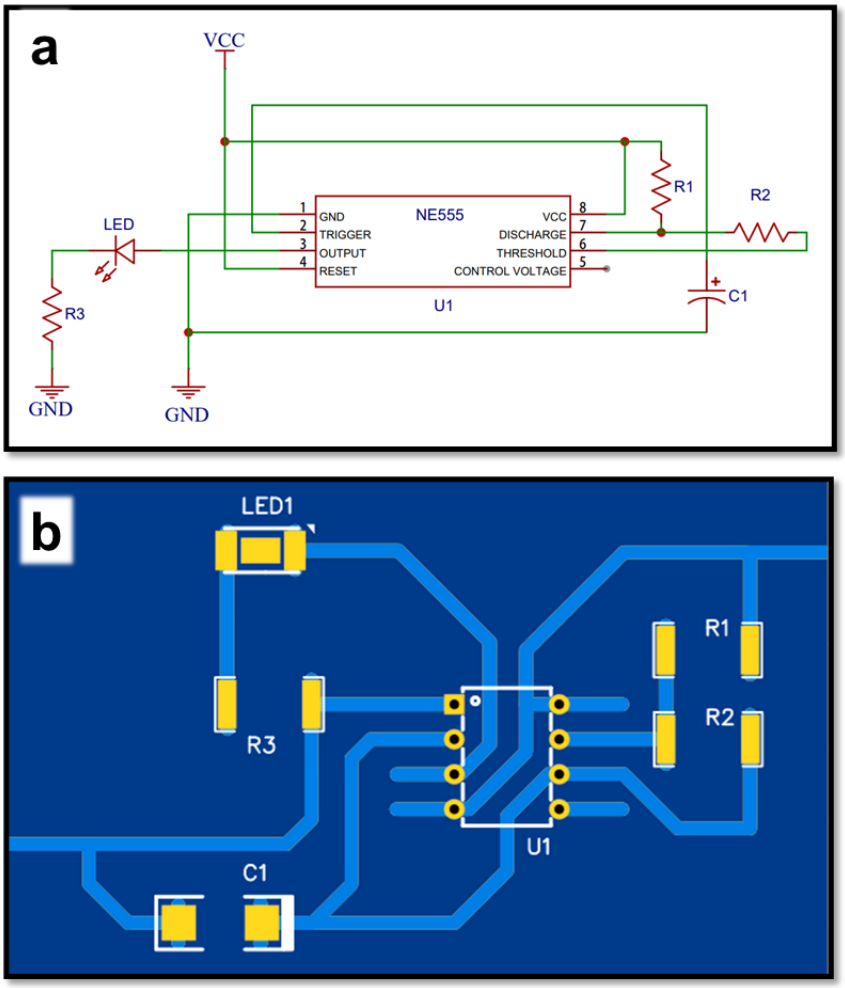

Supplementary Fig. 22 | Design of stroboscopic luminescent circuits. (**a**) Strobe circuit schematic diagram. (**b**) circuit layout diagram based on LMNM. The circuit is driven by 5 V regulated DC power supply (DPS305u). The resistance values of R_1, R_2 and R_3 are 1 kΩ, 10 kΩ and 100 Ω respectively, and the capacitance of C_1 is 47 μF.

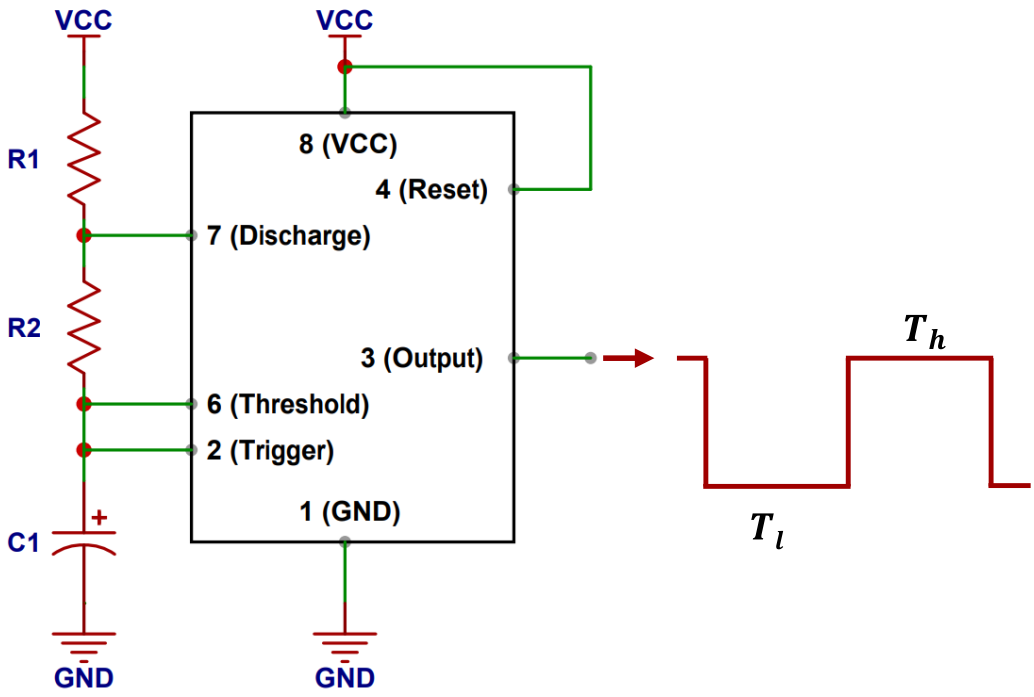

Supplementary Fig. 23 | Schematic diagram of NE555 working in free running mode to output continuous rectangular wave output signal. The frequency *f*, low state time T_l, and high state time T_h of the signal can be calculated by the following equation $f = \frac{1.44}{(R_1+2R_2)C_1}$; $T_l = 0.693R_2C_1$; $T_h = 0.693(R_1 + R_2)C_1$, where R stands for resistance and C for capacitance.

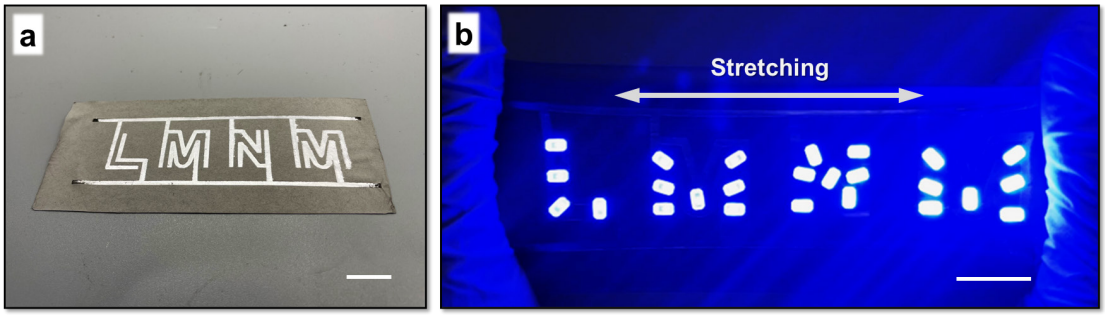

Supplementary Fig. 24 | Stretchable light-emitting array based on LMNM. Digital image of LMNM circuit (**a**) and LED array under stretching condition (**b**). The circuit is obtained by the stamping process in one step, LED bulbs are placed and powered by 3.7 DC power source. Scale bar: 2 cm.

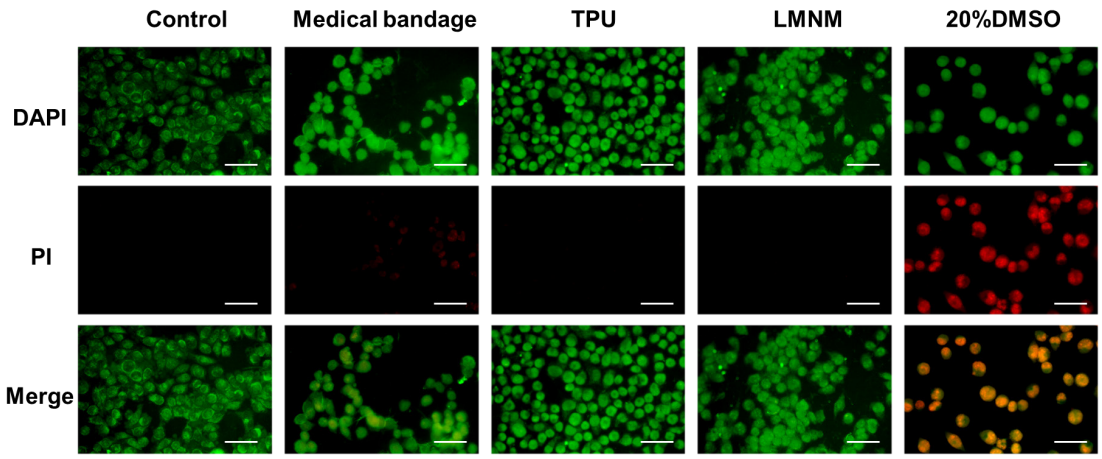

Supplementary Fig. 25 | Fluorescence microscopy images of LIVE/DEAD staining of L929 cells after 24-hour incubation with different groups. Green (DAPI) and red (PI) stains indicate viable and dead cells, respectively. Scale bar: 50 μm. The control, TPU, and LMNM groups exhibited normal cell morphology with minimal cell death. The elastic bandage group showed low toxicity, while the positive control group showed inhibited cell proliferation and a significant increase in cell death.

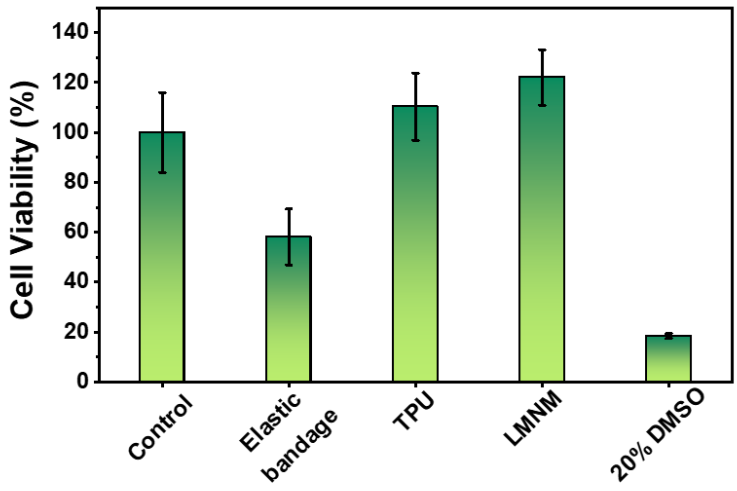

Supplementary Fig. 26 | Quantitative analysis of cell viability in different groups after 24h of incubation. The cell viability was calculated based on the absorbance of CCK-8 assay. The nanofibre structure of TPU and LMNM promoted the proliferation of L-929 cells compared to the control group. The positive control group showed inhibited cell proliferation and a significant decrease in cell viability. Data are presented as mean values ± s.d. (n = 5 biologically independent samples).

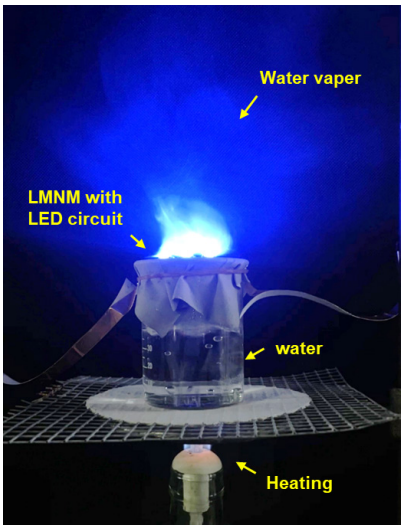

Supplementary Fig. 27 | Demonstration of ventilation and evaporation properties of LMNM circuits equipped with blue LEDs.

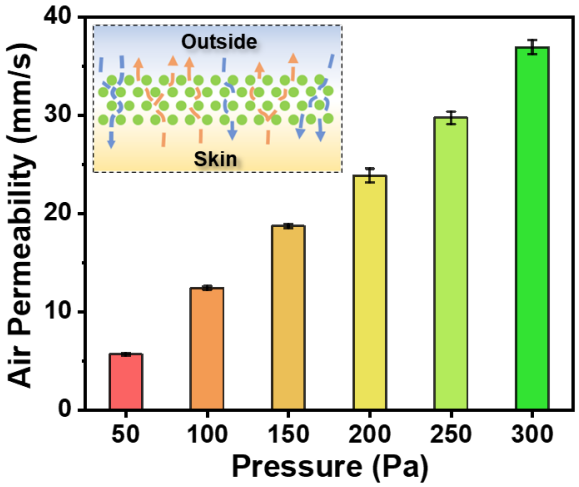

Supplementary Fig. 28 | Differential pressure response to the air permeability of LMNM. The sample size was 10×10 cm^2, and the thickness was 100 μm. The inset represents the direction of airflow between the human skin and the external environment. Data are presented as mean values ± s.d. (n = 5 biologically independent samples).

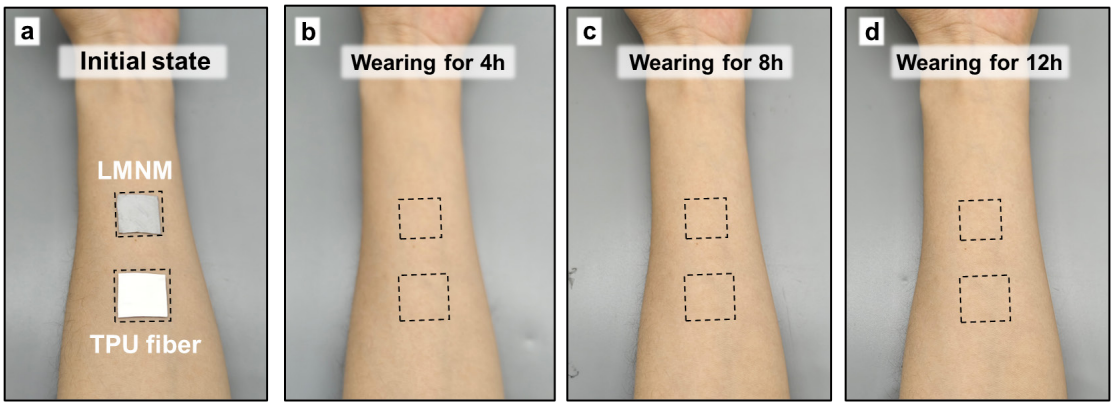

Supplementary Fig. 29 | Compatibility of LMNM with human skin. (**a**) LMNM and TPU nanofibre membranes attached to the upper arm, and the skin surface conditions were recorded after wearing for (**b**) 4 h, (**c**) 8 h, and (**d**) 12 h, respectively. No skin irritant reaction was observed after wearing. The dimensions of the electrodes were 2×2 cm^2.

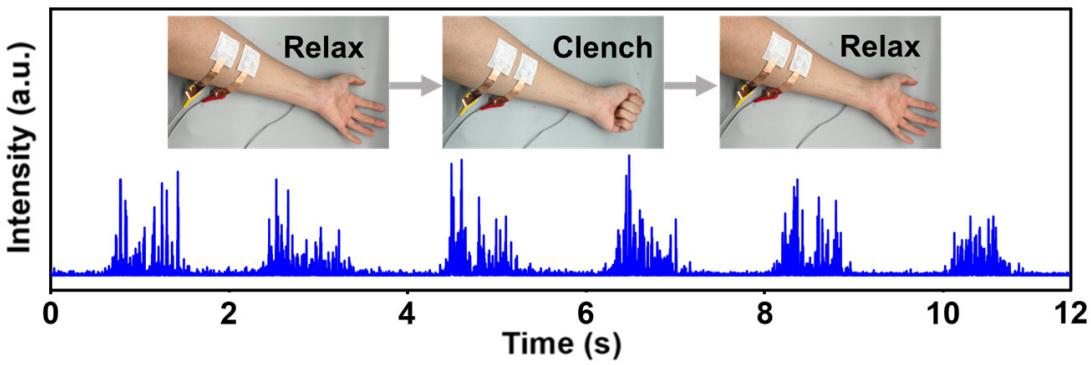

Supplementary Fig. 30 | Electromyography (EMG) signals collection. EMG signal diagram shows muscle activity during 6 clenches in 12 seconds, captured by the LMNM electrode. The inset images show the location of the LMNM on the arm. The dimensions of the LMNM sample were 2×2 cm^2.

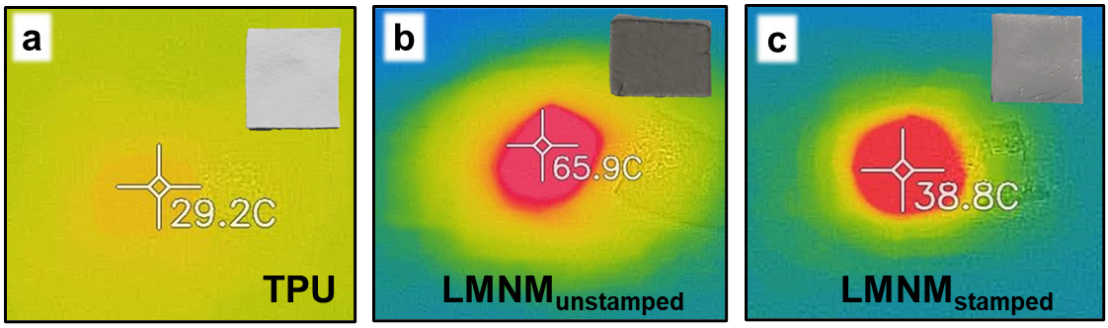

Supplementary Fig. 31 | Photothermal Properties of LMNM. Infrared images of TPU nanofibrous membrane (**a**) and LMNM before (**b**) and after (**c**) stamping under near infrared ray (NIR) laser. The sample size was 2×2 cm^2.

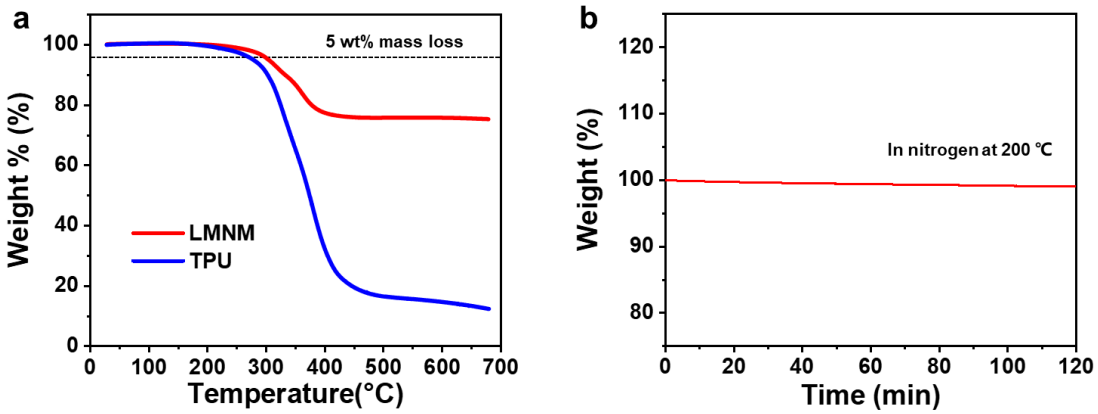

Supplementary Fig. 32 | Thermal stability of LMNM. (**a**) TGA curves of TPU nanofibrous membranes and LMNM under nitrogen environment (heating rate: 10 °C min^{-1}). They are both stable below 300 °C (mass loss less than 5 wt%), sufficient to meet most service conditions. The high mass retention of LMNM reflects its extremely high loading capacity for LM. (**b**) Long-term durability of LMNM at 200 °C in nitrogen.

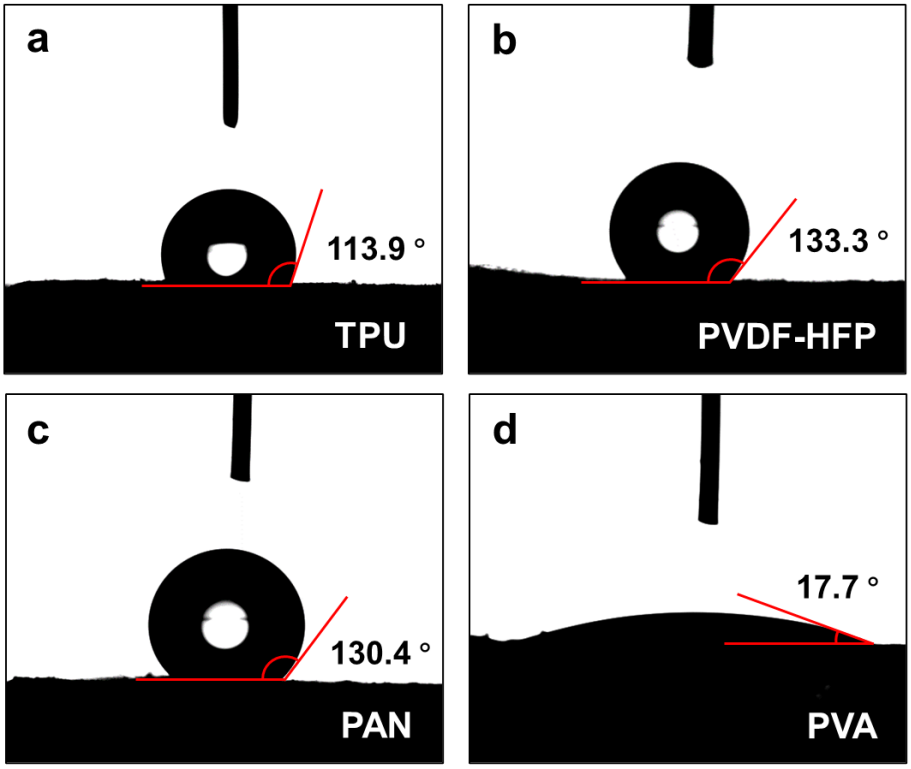

Supplementary Fig. 33 | Digital photographs showing contact angles of LMNM prepared using different polymers. (**a**) thermoplastic polyurethane (TPU), (**b**) poly(vinylidene fluoride-co-hexafluoropropylene) (PVDF-HFP), (**c**) polyacrylonitrile (PAN) and (**d**) poly(vinyl alcohol) (PVA).

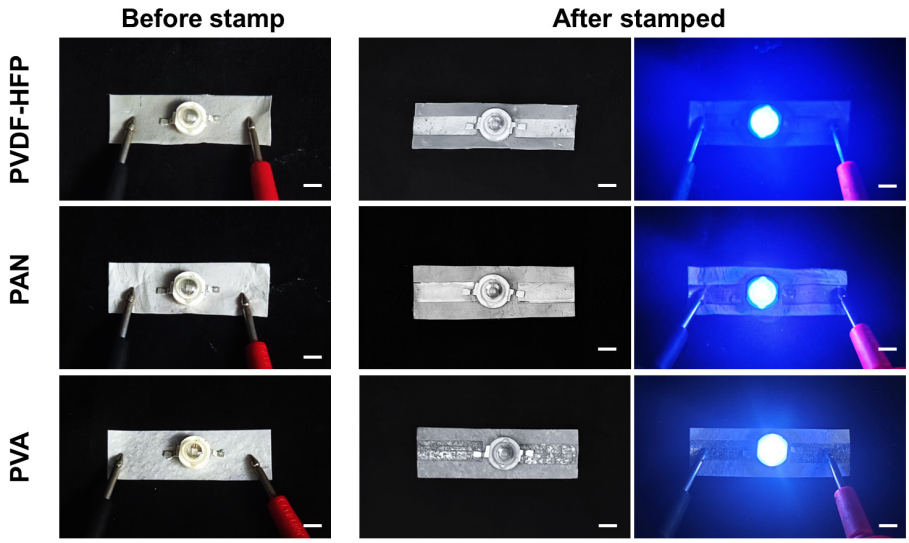

Supplementary Fig. 34 | Digital photographs of conductive pathways constructed on LMNM prepared from different polymers by stamping. The polymers used were poly(vinylidene fluoride-co-hexafluoropropylene) (PVDF-HFP), polyacrylonitrile (PAN) and poly(vinyl alcohol) (PVA), showing the excellent universality of this method. Scale bar: 5 mm.

Ref.	Materials	Methods	Permeability	Minimum line width
This work	**Nanofibre**	**Pressure-stamping**	**Air & moisture**	**50 μm**
Nat. Mater. 2018, 17, 618–624	Membrane	Scribing	None	1000 μm
Adv.Mater.2020, 32, 2002178	Membrane	Screen-printing	None	100 μm
Comm. Mat. 2021, 2:64	Membrane	Embossing	None	250 μm
Nat. Mater. 2021, 20, 859–868	Fibre mat	Scratch coating	Air & moisture	1000 μm
ACS Nano 2021, 15, 19364−19376	Nanofibre	Scratch coating	Air	500 μm
Sci. Adv. 2020; 6 : eabd0202	Membrane	Scratch coating	None	100 μm
Adv. Funct. Mater. 2020, 30, 1910524	Membrane	Scratch coating	None	500 μm
Nat. Mater. 2021, 20, 851–858	Membrane	Spraying and sintering	None	400 μm
Adv. Funct. Mater. 2019, 29, 1808739	Membrane	Spray coating	None	200 μm
Nat. Commun. 2019, 10, 3514.	Nanofibrils	Sintering	None	N.A.
Sci. Adv. 2021; 7 : eabg4041	Core-shell fibre	Stretching	None	N.A.
Adv. Mater. 2019, 31, 1903864	Acrylate binder	Stretching	None	N.A.

Supplementary Table 1 | The performance comparison with representative liquid metal base flexible electronics that have been reported in recent years.

Reference

1. H. A. Stone, Low reynolds number motion of bubbles, drops and rigid spheres through fluid-fluid interfaces. *J. Fluid Mech.* **287**, 279–298 (1995).
2. B. K. Brettmann, S. Tsang, K. M. Forward, G. C. Rutledge, A. S. Myerson, B. L. Trout, Free surface electrospinning of fibers containing microparticles. *Langmuir*. **28**, 9714–9721
3. R. W. Style, R. Boltyanskiy, B. Allen, K. E. Jensen, H. P. Foote, J. S. Wettlaufer, E. R. Dufresne, Stiffening solids with liquid inclusions. *Nat. Phys.* **11**, 82–87 (2015).
4. Eshelby, J. D. The determination of the elastic field of an ellipsoidal inclusion, and related problems. Proc. R. Soc. Lond. A **241**, 376–396 (1957).
5. Brisard, S., Dormieux, L. & Kondo, D. Hashin–Shtrikman bounds on the bulk modulus of a nanocomposite with spherical inclusions and interface effects. Comput. Mater. Sci. **48**, 589–596 (2010).